Rover-Mounted Radar Observation of Discrete Layers Within the Top 4 Meters of Regolith at the Chang'E-3 Landing Site, the Moon

Chunyu Ding, Yiren Chang, Yan Su, Jiawei Wang, and Minggang Xie

***Abstract*— The radar equipment carried by the Chang'E-3 (CE-3) mission marked the first deployment of rover-mounted ground-penetrating radar (GPR) to observe the lunar surface. This provided an unparalleled opportunity for a high-resolution investigation into the fine structure of the lunar regolith. This article has revealed the presence of multiple discrete layers within the top 4 m of the lunar regolith using high-frequency radar data from the CE-3 Yutu rover. Subsequently, we have established realistic models of the lunar regolith to obtain the radar simulation calculated by finite-difference time-domain (FDTD) technology. Thus, we compare the simulated radar data with actual observational data to comprehensively confirm the existence of multiple discrete layers within the lunar regolith. Taking into consideration the geological context of the CE-3 landing site and the principles of impact crater formation, we infer that the origin of the multiple discrete layers within the top 4 m of the CE-3 landing site is likely the by-product of multiple depositions of ejecta from nearby small craters. Our findings suggest the possibility of the widespread existence of multiple discrete layers within the lunar regolith and emphasize the significant contribution of ejecta from small impact craters to the accumulation of local lunar regolith thickness on the Moon's surface.**

***Index Terms*— Chang'E-3 (CE-3) mission, lunar exploration, lunar regolith, Moon-based ground-penetrating radar (GPR), planetary remote sensing, subsurface structure.**

Manuscript received 9 October 2023; revised 31 December 2023; accepted 7 February 2024. Date of publication 12 February 2024; date of current version 23 February 2024. This work was supported in part by the National Natural Science Foundation of China under Grant 42241139, Grant 12203036, Grant 62227901, and Grant 42004099; in part by the Opening Fund of the Key Laboratory of Lunar and Deep Space Exploration, Chinese Academy of Sciences (CAS), under Grant LDSE202005; in part by the Fund of Shanghai Institute of Aerospace System Engineering under Grant PZ_YY_SYF_JY200275; and in part by the Shenzhen Municipal Government Investment Project under Grant 2106-440300-04-03-901272. *(Corresponding author: Chunyu Ding.)*

Chunyu Ding and Jiawei Wang are with the Institute for Advanced Study, Shenzhen University, Shenzhen 518960, China (e-mail: dingchunyu@szu.edu.cn; 2021191218@email.szu.edu.cn).

Yiren Chang is with the Shanghai Key Laboratory for Astrophysics, Shanghai Normal University, Shanghai 201109, China (e-mail: changyiren@shnu.edu.cn).

Yan Su is with the Key Laboratory of Lunar and Deep Space Exploration, National Astronomical Observatories, Chinese Academy of Sciences, Beijing 100012, China, and also with the School of Astronomy and Space Science, University of Chinese Academy of Sciences, Beijing 100049, China (e-mail: suyan@bao.ac.cn).

Minggang Xie is with the School of Physics and Electronic Information Engineering, Guilin University of Technology, Guilin 541004, China (e-mail: xieminggang@glut.edu.cn).

Digital Object Identifier 10.1109/TGRS.2024.3365130

I. Introduction

THE Moon is Earth's closest neighbor and serves as humanity's primary target for venturing beyond Earth into deep space [1], [2]. When it comes to human exploration of the Moon, the most immediate and essential objective is the lunar regolith [3]. The lunar regolith is a loose material covering the entire surface of the Moon, formed over time as a result of meteorite impacts and weathering [3]. Studying lunar regolith enables us to gain a better understanding of the evolutionary history of the Moon's shallow subsurface.

The thickness of the lunar regolith varies unevenly across the globe on the Moon [4]. Typically, it is approximately 5 m thick in lunar mare regions, whereas it reaches around 10 m thick in highland areas [5], [6]. Since optical methods lack penetration capability, they can only indirectly infer the internal structure of lunar regolith from imagery [4]. The most direct means for studying the interior structure and thickness of lunar regolith include drilling, seismic studies, and radar observations [7], [8], [9], [10], [11], [12], [13], [14]. The deepest core samples obtained through drilling were from the Apollo 17 mission, reaching a depth of ∼3 m [15]. However, it still did not penetrate through the regolith to reach the bedrock, particularly since the regolith thickness is typical ∼5 m in lunar mare regions [6]. Seismic methods suffer from limited vertical resolution, making it challenging to discern the internal structure of the shallow subsurface regolith [11], [14]. Similarly, orbiting-based radar observations of the lunar subsurface, such as the Lunar Radar Sounder (LRS) on Japan's Kaguya mission and the Apollo Lunar Sounder Experiment (ALSE) radar on Apollo 17, are constrained by spatial resolution limitations [16], [17]. These orbiting-based radars struggle to probe the internal structure of shallow subsurface regoliths. However, the Chinese Chang'E-3 (CE-3) mission became the first to carry an in situ Moon-based ground-penetrating radar (GPR) to observe the Moon's surface [10], [18], [19]. It was deployed in the northeastern part of the Mare Imbrium on the near side of the Moon [20]. This in situ radar marked a pioneering step in extraterrestrial GPR observations and provided an opportunity for high-resolution insights into the internal structure of lunar regolith's shallow subsurface.

In 2013, China's CE-3 spacecraft touched down approximately 50 m east of the rim of the Ziwei crater [Fig. 1(a)], which has a diameter of 450 m [18], [19]. The Apollo 17 mission landed in the Mare Tranquillitatis [Fig. 1(d)] on

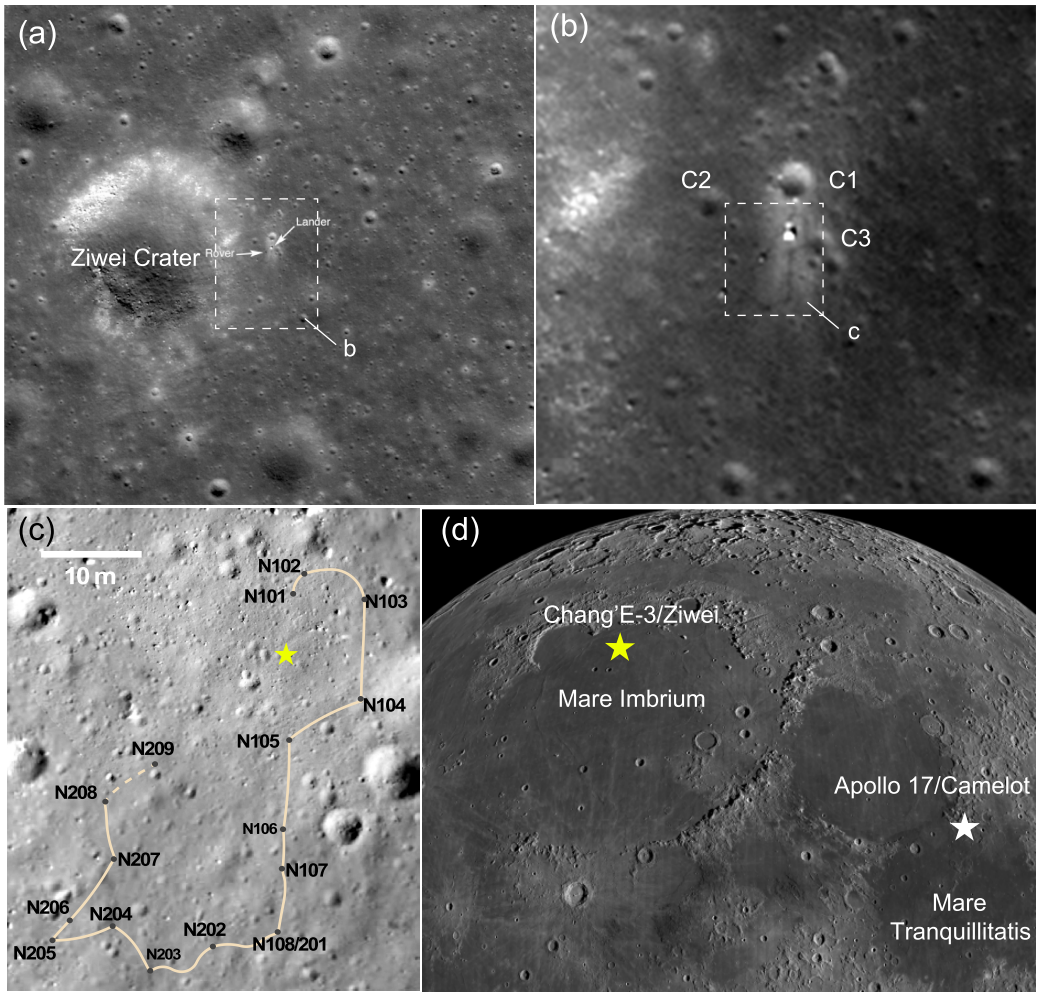

Fig. 1. Geological background of the CE-3 landing site and the Yutu rover traversal route. (a) CE-3 landing site is located in the northeastern province of the Mare Imbrium, with coordinates at 44.1214°N, 19.5117°W [21]. The landing site is situated to the east of the 450-m-diameter Ziwei crater. White arrows indicate the positions of the Yutu rover and the lander. The base map is sourced from Lunar Reconnaissance Orbiter Camera Narrow Angle Camera (LROC NAC) imagery (image ID: M1142582775R). (b) Zoomed-in image of the landing site, with black shadows representing the path of the lunar rover. Surrounding the lander, there are several small craters, such as C1, C2, and C3. The base map is sourced from LROC NAC (Image ID: M1147290066R). (c) Traveling map of the Yutu rover's route, with the light yellow segments indicating the rover's path during its first two lunar days. Black dots on the segments represent navigation points, with N denoting navigation point and 1 signifying the first lunar day. The base map is sourced from the CE-3 lander's descent camera data (image ID: CE3_BMYK_LCAM-3006). (d) Relative positions of the Ziwei crater in the CE-3 landing area and the Camelot crater in the Apollo 17 landing area.

the near side of the Moon in 1972 [22]. Its landing site was situated approximately 600 m east of the rim of the Camelot crater, which has a diameter of 650 m [23]. The Apollo 17 mission drilled and sampled lunar material to a depth of ~3 m at the landing site [15], whereas the CE-3 landing area has been observed to be approximately 10 m deep beneath the lunar surface using a high-frequency in situ GPR [24], [25]. Both missions landed on ejecta from impact craters of similar sizes, providing an opportunity for comparative studies of the internal structure of lunar regolith in similar crater settings. Previous studies have primarily focused on various aspects of lunar subsurface structure using CE-3 radar data, including stratigraphy beneath the landing site [19], [20], [25], [26], [27], the dielectric constant and loss tangent of lunar regolith [28], [29], in situ helium-3 resources within lunar regolith [24], and unique geological features, such as subsurface cavities [30]. However, there has been limited research on fine-scale structures within lunar regolith, such as layering structures within the regolith, which was observed by the core sample collected by previous Apollo missions, and the thickness of each layering structure is approximately 4–5 cm [3]. For instance, the CE-3 high-frequency radar preliminarily observed the presence of multiple layers within the shallow lunar regolith, with a dielectric constant constrained to be between 4.5 and 5.5, which has been interpreted as a material intermediate between lunar regolith and solid basalt [18]. Apollo core samples revealed the presence of tens of layers within the first few meters of lunar regolith, but consensus on whether these discrete layered structures are widespread within lunar regolith and their nature has not been reached [15], [31], [32].

This article investigates the discrete layered structures within the lunar regolith observed by the high-frequency GPR data from the CE-3 mission. Based on finite-difference time-domain (FDTD) numerical simulation and comparison with actual radar observation, we confirm the presence of numerous horizontally discontinuous discrete layered structures within the lunar regolith to a depth of approximately

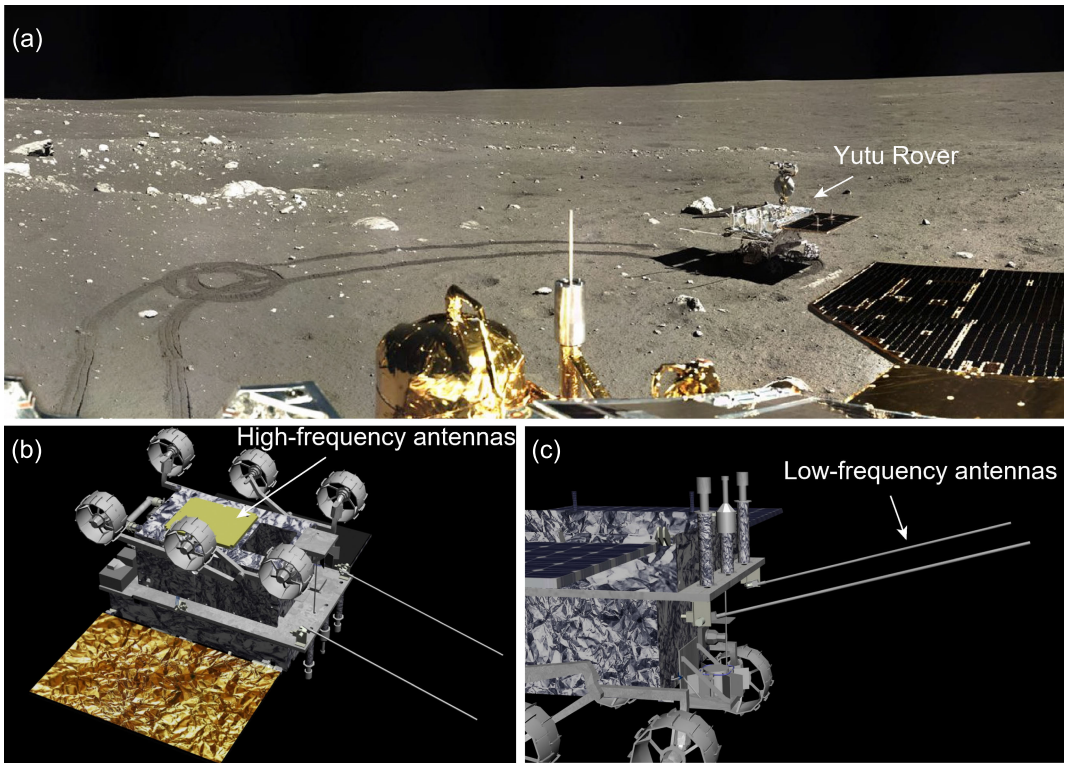

Fig. 2. Moon-based GPR surface deployment for in situ lunar detection, featuring the radar comprising both high- and low-frequency channels. (a) Scenario of the Yutu rover carrying the radar for surface exploration on the Moon's surface, captured by the lander's camera. (b) High-frequency channel of the radar is mounted on the bottom of the Yutu rover and consists of bow-tie antennas. (c) Low-frequency channel of the radar is installed at the rear of the Yutu rover and consists of dipole-shaped antennas.

4 m. In addition, we compare our findings with studies based on drilling and sampling data from the Apollo 17 mission. Our analysis leads to the inference that discrete layered structures are likely to be widespread geological features within lunar regolith. The origin of these discrete layers is believed to be attributed to ejecta from smaller craters at different time intervals in the surrounding area. The structure of this article is given as follows. First, we provide an introduction to radar exploration of the CE-3 mission (see Section II-A) and the radar observational data collected on the lunar surface (see Section II-B). Second, we describe the methodology for modeling the lunar regolith and its corresponding numerical calculation method (see Section II-C), along with the approach for similarity calculation for the radar observation and simulation (see Section II-D). Third, we present the comparison results between high-frequency radar observations and simulations (see Section III). Fourth, we discuss whether fragmented boulders within the lunar regolith can form the horizontal layered structures seen in radar images (see Section IV-A) and conduct a comparative analysis between the CE-3 landing area and the Apollo 17 landing area (see Section IV-B). Finally, we explore the origins of discrete layers within the lunar regolith and update the interpretation of regolith stratigraphy at the CE-3 landing site (see Section IV-C).

II. Yutu Radar, Data, and Methods

A. Yutu Radar Descriptions

The in situ GPR carried by the CE-3 mission is a time-domain pulse radar [10]. This GPR is mounted on the Yutu rover [see Fig. 2(a)] and consists of two channels, the low- and high-frequency channels, also referred to as the first channel and the second channel [10]. The central frequency of the first channel is 60 MHz, with a bandwidth of 20–80 MHz and a vertical resolution at the meter level. Its primary scientific objective is to detect geological structures beneath the lunar subsurface at depths greater than 100 m [33], [34]. The first channel is installed at the rear of the Yutu rover, as shown in Fig. 2(c). The central frequency of the second channel is 500 MHz, with a bandwidth of 250–750 MHz and a vertical resolution better than 0.3 m [10], [33], [35]. It is primarily used to investigate the fine structure and thickness of the lunar regolith [see Fig. 2(b)]. The second channel consists of three bow-tie antennas, with one antenna transmitting the signal, while the other two antennas receive the data, and the spacing between the antennas is ∼0.16 m [10], [36]. Consequently, the high-frequency channel effectively receives two sets of radar echo signals, identified as CH2A and CH2B.

B. Data Collections

The Yutu rover of the CE-3 mission, due to mechanical malfunctions, was unable to move during the third lunar day after landing on the Moon. Therefore, the GPR carried by the Yutu rover covered a total distance of approximately 114 m on the lunar surface, from Navigation Point N101 to N209, as shown in Fig. 1(c) [18], [19], [26]. Fig. 3(a) labels images captured by the panoramic cameras mounted on the CE-3 lander showing a scenario of radar survey on the Moon's surface. The terrain in the CE-3 landing area is relatively smooth, with an average slope of ∼1.7%, which is conducive

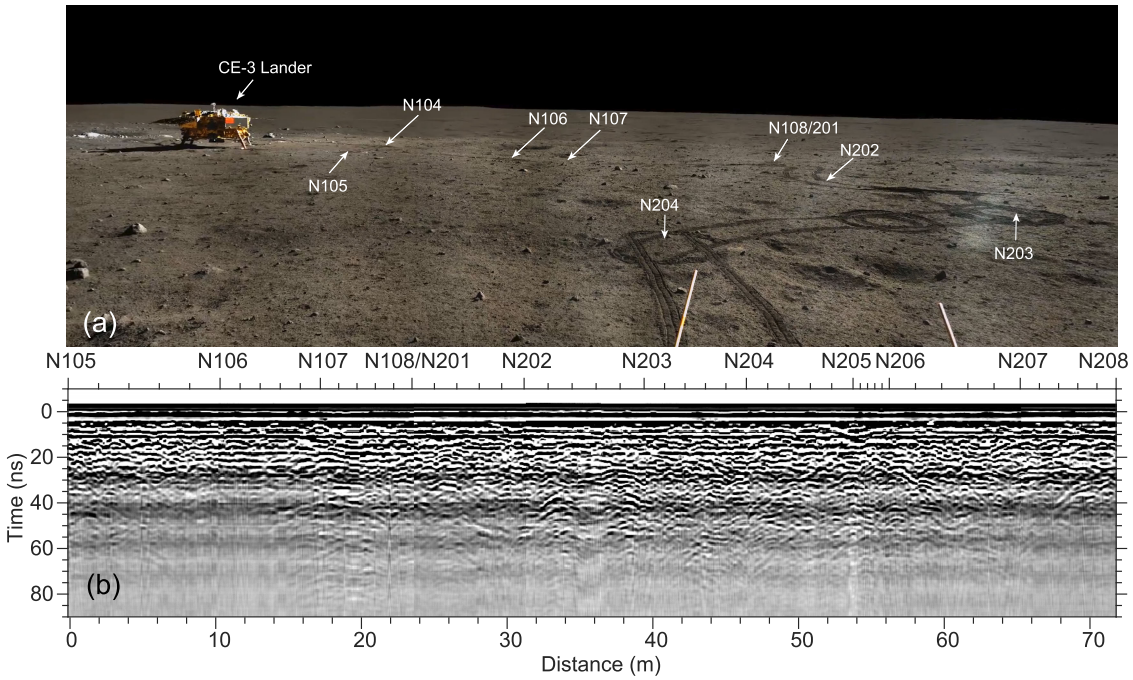

Fig. 3. (a) Yutu rove's tracks left on the lunar surface during its exploration, with corresponding navigation point locations marked by the white arrows. (b) Radargram was collected by the high-frequency channel of the GPR between navigation points N105 and N208.

to the rover's traversal on the lunar surface [37]. Throughout the Yutu rover's travel, the GPR remained functional. However, radar data were lost between navigation points N208 and N209, resulting in a total radar data coverage of approximately 107.4 m within the landing area [18].

In the initial phase of lunar surface exploration, the GPR was used to adjust the radar system's parameters. For instance, the system gain for the radar was varied between N101 and N105, with gain values of 31 dB, a fixed gain of 50 dB, and variable gains of 20 and 10 dB. Consequently, there were variations in the radar signal penetration depth between N101 and N105, leading to some inconsistencies in the radar images. However, from N105 to N208, a consistent variable gain of 0 dB was employed, resulting in more uniform and continuous radar data. Therefore, we utilized the high-frequency radar data (Level 0B) covering approximately 74.2 m between N105 and N208 used in this study. Here, we performed preprocessing tasks including direct current (dc) component removal, physical quantity conversion, and elimination of redundant data, as shown in Fig. 3(b).

C. Lunar Regolith Models and FDTD Simulations

To validate the observed discrete layered structures within the lunar regolith in the high-frequency radar data, we employed the random medium algorithm to construct the lunar regolith model and used the FDTD technique to calculate numerical simulation results from the model. Finally, we compared the actual observation data with the simulation data to confirm the existence of discrete layered structures. Typically, traditional models of lunar regolith assume a homogeneous and single-material composition. However, the actual internal structure of the lunar regolith is complex, with internal media exhibiting anisotropy. Therefore, in the process of building the lunar regolith model in this article, we aimed to simulate the distribution of the internal structure and its dielectric properties. The modeling process was completed in the following steps.

1) We utilized a random medium model to establish the spatial variations in the dielectric properties of lunar regolith material, such as dielectric constant and loss tangent.
2) Based on findings from Apollo samples indicating that lunar regolith density increases with depth [38].
3) Extraction of horizontal reflection structure based on the characteristics of echo signals in radargrams.

1) Random Medium Modeling: A random medium model consists of large-scale inhomogeneities and small-scale inhomogeneities [39]. The large-scale inhomogeneities are used to describe the average characteristics of the medium and are represented by means. The small-scale inhomogeneities are random perturbations added to the model and are characterized by statistical properties such as spatial autocorrelation functions, autocorrelation lengths, and perturbation standard deviations. In lunar GPR exploration, electromagnetic waves are primarily influenced by the dielectric constant and loss tangent as they propagate through the subsurface medium [13], [40].

Under the assumption of a stationary random process, the dielectric constant of the random medium model is expressed by the following equation:

$$\varepsilon(x,z) = \varepsilon_m + \delta(x,z) \cdot \varepsilon_f(x,z) \tag{1}$$

where ε_m represents the background large-scale perturbation; $\delta(x,z)$ represents the model standard deviation; and $\varepsilon_f(x,z)$ represents the small-scale random perturbation, with its spatial distribution characteristics following an

autocorrelation function. In this context, the autocorrelation function is employed to characterize the degree of correlation and inherent relationship of the dielectric constant in various spatial locations within the random medium, making it better align with the actual spatial distribution characteristics of the dielectric constant. Autocorrelation functions that are frequently used include types such as Gaussian and exponential [41]. The Gaussian-type autocorrelation function is mainly used to describe single-scale smooth inhomogeneous media, while the exponential-type autocorrelation function is employed to describe inhomogeneous media with multiscale and self-similar characteristics. We adopted an autocorrelation function to describe the lunar regolith model, expressed as follows:

$$r(x,z) = e^{-\left[\left(\frac{x}{a}\right)^2+\left(\frac{z}{b}\right)^2\right]^{\frac{1}{1+r}}} \tag{2}$$

where a and b represent the horizontal and vertical autocorrelation lengths of the random medium, respectively. r determines the nature of the autocorrelation function. For instance, when $r = 0$, the autocorrelation function becomes Gaussian-type, and when $r = 1$, it becomes an exponential-type autocorrelation function [42].

In practical modeling, computers cannot simulate infinite areas. Therefore, it is necessary to discretize the continuous random medium models within a finite range. This article provides a discrete modeling method for the lunar regolith random model, with the algorithmic steps as follows [43].

1) First, we need to determine the selected autocorrelation function, specify the range of the regolith model, and set the parameter values.
2) Subsequent, by applying the Fourier transform to the autocorrelation function, we can derive its power spectral density function, expressed as

$$R(x,z) = \sum_{x=0}^{M-1}\sum_{t=0}^{N-1} r(x,z)e^{-j2\pi\left(\frac{k_x x}{M}+\frac{k_z z}{N}\right)}. \tag{3}$$

3) Third, we add random components to the power spectral density function of the autocorrelation function. The outcome is the power spectral function that is random and can be expressed in the following form:

$$W(x,z) = \sqrt{R(x,z)}\cdot e^{j\varphi(x,z)} \tag{4}$$

where $\varphi(x,z)$ is the random phase function, with its values belonging to an independent, and it is a uniformly distributed random sequence within the interval $[0, 2\pi)$.
4) Thereon, by performing the inverse Fourier transform of the random power spectral function, we can obtain the spatial perturbation function of the random medium, shown as

$$\varepsilon_f(x,z) = \frac{1}{MN}\sum_{k_x=0}^{M-1}\sum_{k_z=0}^{N-1} W(x,z)e^{j2\pi\left(\frac{k_x x}{M}+\frac{k_z z}{N}\right)}. \tag{5}$$

5) Finally, by substituting (6) into (1), we can obtain the random medium model of the lunar regolith.

2) Profiles of the Variation in Dielectric Constant at Different Depths in the Landing Area: Building upon the lunar regolith random model, we introduce depth-dependent density profiles in the vertical direction. Density profiles obtained from Apollo drill core samples, covering approximately 3 m beneath the lunar surface, have been commonly used in constructing lunar regolith layer models [35], [44]. However, different geological units exhibit varying degrees of weathering within their internal lunar regolith, leading to differences in the depth-dependent density variations [40]. The CE-3 mission did not acquire on-site drill core samples of the shallow lunar regolith within the landing area. Instead, the high-frequency channel GPR carried by the Yutu rover obtained observational data for several meters beneath the lunar surface [24], [26]. These radar observation data have been used to inverse the distribution of the lunar regolith's dielectric constant with depth [26], [27], [29], [45].

Typically, buried rock fragments beneath the lunar surface in radar images exhibit hyperbolic characteristics. By constructing an electromagnetic wave propagation model based on the features of these hyperbolic curves, the radar electromagnetic wave's velocity in the lunar regolith can be calculated, leading to the determination of the dielectric constant. This method is known as the hyperbolic fitting method and is widely used for dielectric constant estimation in lunar and Martian GPR studies [18], [26], [46]. Here, we employ the profiles of electromagnetic wave velocity with respect to time obtained from the CE-3 radar observation, as shown in Fig. 4(a) [18], [24]. In Fig. 4(a), the blue curve represents the fit average velocity variation over time, while the yellow curve represents the interval velocity variation over time, transformed using Dix's formula as follows [47]:

$$\hat{v}_n = \sqrt{\frac{t_n v_n^2 - t_{n-1}v_{n-1}^2}{t_n - t_{n-1}}} \tag{6}$$

where v represents the average velocity and t denotes the time. To adapt to the construction of the lunar regolith model, we further transform the curve of interval velocity variation over time into a curve of dielectric constant variation with depth using the formula, $c = (\varepsilon)^{1/2}\cdot v$. The transformed result is represented by the black dots in Fig. 4(b). We attempted to fit the black dots in Fig. 4(b) with both first- and second-order curve functions, resulting in the blue and yellow curves shown in Fig. 4(b), respectively. The relative errors between the fit curves (blue and yellow curves) and the fit values (black dots) are ~1.07% and ~0.50%, respectively. The performance of the second-order function fitting is superior to that of the first-order function. Therefore, we adopted the results of the second-order function fitting, and the curve formula is expressed as follows:

$$\varepsilon(z) = 4.64\frac{z^2+0.60z+0.30}{z^2+0.61z+0.65} \tag{7}$$

where z represents depth in meters. The black curve in Fig. 4(b) corresponds to the fitting curve for Apollo samples, and its formula is given as [38]

$$\varepsilon(z) = 1.919^{1.92\frac{z+12.2}{z+18}} \tag{8}$$

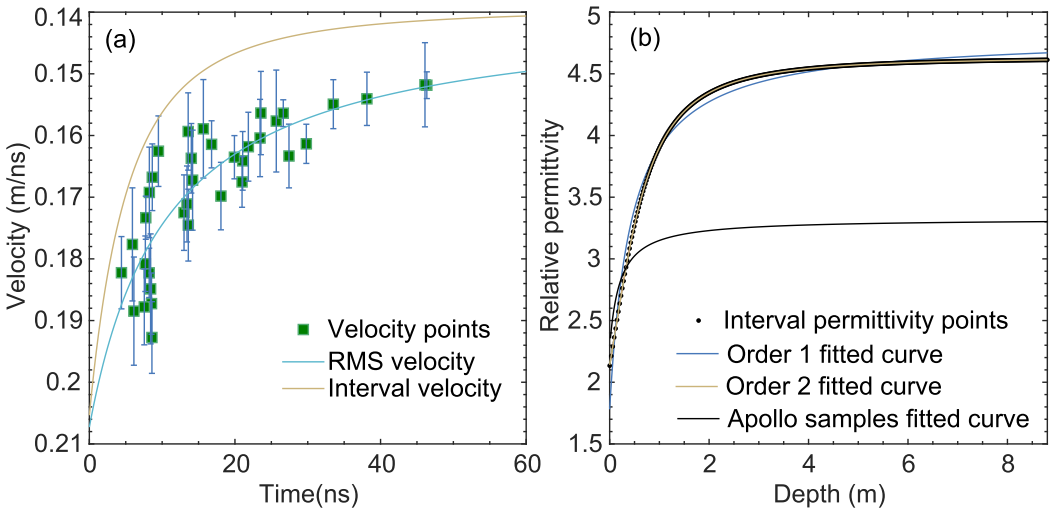

Fig. 4. (a) Estimation of radar electromagnetic wave propagation velocity in the lunar regolith using the hyperbolic fitting method. The green dots represent the radar electromagnetic wave velocities in the lunar regolith at different time intervals, the blue lines represent the average velocity curve fit using the least-squares method, and the yellow lines represent the fit interval velocity curve. (b) Comparison of depth-dependent profiles between lunar regolith in the CE-3 landing site and Apollo regolith samples.

where z represents depth in meters. It can be observed that the distribution of dielectric constants in the shallow lunar regolith within the CE-3 landing area is slightly higher than that within the Apollo regolith samples laboratory measured result. This discrepancy may be attributed to the fact that the geologic unit areas where Apollo samples were collected are older than the CE-3 landing area, indicating a higher degree of weathering within the lunar regolith.

3) Identifying Discrete Layered Structures in Radargram: The discrete layered structures were extracted from the lunar radar data using a combination of manual and automatic methods. The specific extraction steps are given as follows.

1) First, the envelope signal of the A-scan data was obtained using the Hilbert transform.
2) Second, the peak values of the envelope signals for each A-scan data were extracted.
3) Third, a 2-D distribution map of these peak values was generated.
4) Finally, manual removal of hyperbolic reflection features caused by rocks or other materials was performed to identify the lunar regolith discrete layered structures in the radargram.

4) Construction of the Lunar Regolith Models and Forward Calculation: The initial input for establishing the lunar regolith model was the gained overall dielectric constant and loss tangent. Then, the extracted discrete layered structures are incorporated into the model. Due to the limited vertical resolution of the high-frequency channel radar (better than 0.3 m), it is not possible to constrain the thickness of each discrete layer. Therefore, based on prior knowledge from Apollo missions, this study sets the thickness of each layer to 0.05 m. The dielectric constant of the discrete layered structures has been previously constrained to approximately 5.5 [18], and this value was used in our model. The loss tangent of the lunar regolith at the CE-3 landing site is constructed to 0.011–0.017 by the frequency shift method [28]. Those values are also considered the actual regolith's properties by setting in the lunar regolith model.

Fig. 5 illustrates the construction process of a lunar regolith model with a size of 6.5 × 5 m and its internal discrete layered structure. In Fig. 5(a), the dielectric constant gradually increases with depth, following the depth-dependent profile obtained from actual observations in the CE-3 landing area. In addition, a random medium model is introduced to control perturbations in the horizontal and lateral dielectric constants, aligning them more closely with those of the actual distribution of lunar regolith [see Fig. 5(d)]. The input parameters for the random model are given as follows: $r = 0$ (indicating a Gaussian random model); horizontal and vertical self-correlation lengths set to 75 and 3.75 cm, respectively. In the vertical direction, the model is divided into 20 evenly spaced regions to simulate the dielectric constant's inhomogeneous in that direction. The perturbed background dielectric constant is ∼3.2, with a perturbation standard deviation of ∼18.8%, matching the radar's actual observed results at the CE-3 landing site [18].

Subsequently, we employ the method described in section II-C3 to extract the radar image's discrete layered structure, resulting in the model depicted in Fig. 5(b). In this figure, the dielectric constant of the discrete layered structure is set to 5.5, consistent with observed values [18]. We then combine the models from Fig. 5(a) and (b) to obtain the final lunar regolith model shown in Fig. 5(c). Fig. 5(e) demonstrates the inhomogeneous of the lunar regolith model in the horizontal direction, controlled by the parameters of the random model.

Once the lunar regolith model is constructed, we employ the FDTD technique to perform forward modeling and obtain numerical simulated radar images. The excitation source used for numerical simulation resembles an ultrawideband Ricker wavelet. This waveform is similar to the one radiated by Channel 2 antennas as extracted in the laboratory measurement [10]. The time window for simulating radar data is set to 100 ns, and the grid is partitioned into 0.01-m intervals.

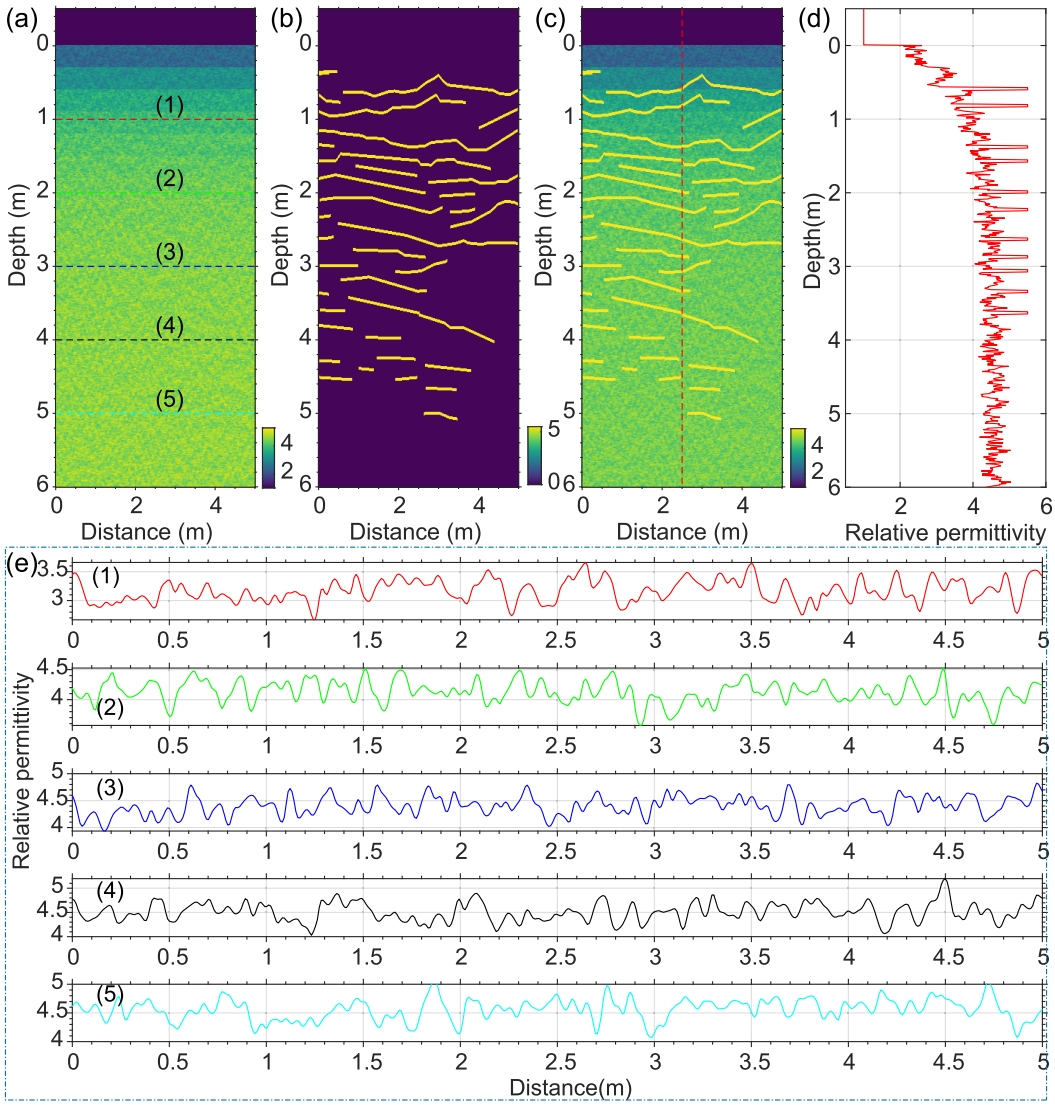

Fig. 5. Construction of the lunar regolith discrete layered structure models. (a) Random regolith medium model with dimensions of 6.5 × 5 m. The first layer represents the vacuum layer with a thickness of 0.5 m. The second layer represents the lunar regolith with a thickness of 6 m. The antenna is positioned 0.3 m above the lunar surface and within the vacuum. (b) Discrete layered structures with an assigned dielectric constant of 5.5 [18]. (d) 1-D variation of dielectric constant with depth in the lunar regolith model, represented by the red dashed line in (c). (e) Horizontal distribution of dielectric constant in the model, illustrating the lateral heterogeneity of the lunar regolith's dielectric constant.

Finally, we calculate the similarity between observed and simulated data using the cosine similarity coefficient in practical computations.

D. Similarity Calculation

To quantify the similarity between the lunar GPR data and simulated data, we employed a straightforward approach known as cosine similarity [48]. The calculation of cosine similarity is given as follows:

$$\cos(A, B) = \frac{\sum_{n=1}^{n} \alpha(\chi_i)\beta(\chi_i)}{\sqrt{\sum_{n=1}^{n} \alpha^2(\chi_i)}\sqrt{\sum_{n=1}^{n} \beta^2(\chi_i)}} \tag{9}$$

where A and B are two vectors representing histograms of the lunar GPR data and simulated data, respectively. The values of cosine similarity fall within the range of 0 to 1. When the values are closer to 1, it indicates that the cosine intersection angle between the two radargrams is closer to 0, implying a higher degree of similarity between the compared radargrams. Therefore, the degree of similarity between the radargrams can be determined based on the cosine similarity value.

III. Results

The results obtained from Apollo core drilling samples have indicated the presence of discrete layered structures within the shallow lunar regolith, extending up to 3 m deep, with several layers ranging from a few to dozens of layers [15], [31], [32]. High-frequency radar data from the CE-3 mission have preliminarily confirmed the existence of the discrete layered structures within the shallow lunar regolith [18]. However, our previous research did not consider the spatially random distribution of lunar regolith properties within the lunar regolith model, and the radar simulations were limited to only two end numbers and did not encompass the entire CE-3 radar observation dataset. In this study, as described in Section II-C, we introduced a distribution of random media within the lunar

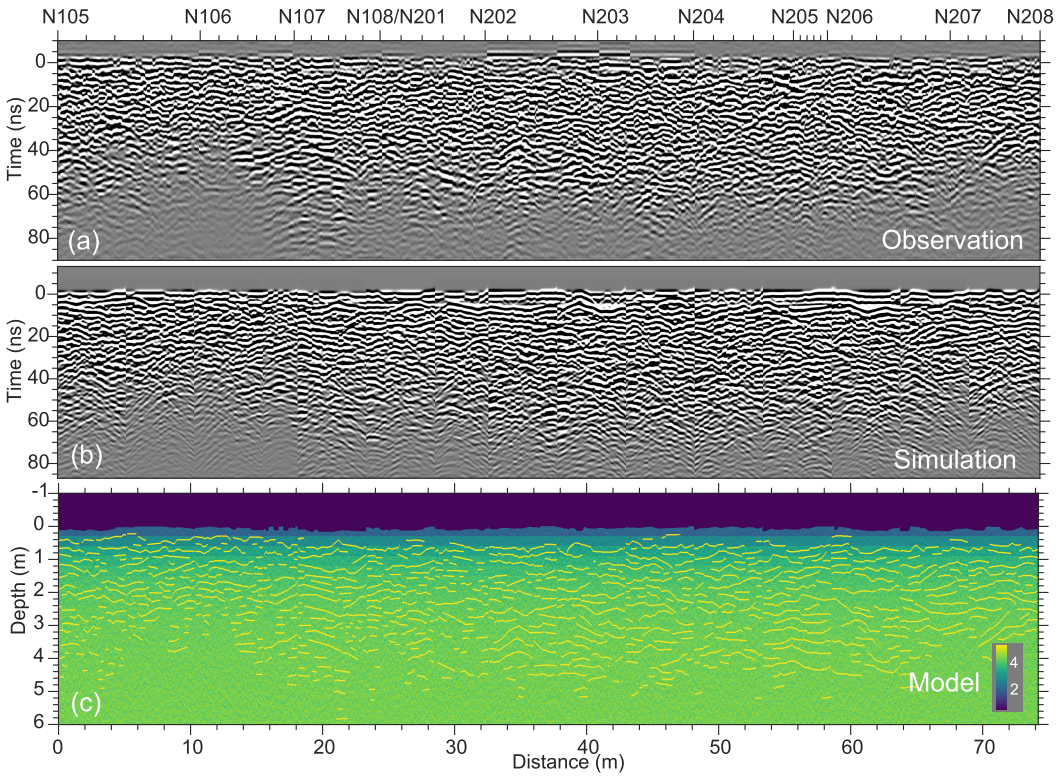

Fig. 6. High-frequency CE-3 radar observation and simulation. (a) High-frequency radar observation data between navigation points N105 to N208; the horizontal axis represents the distance (m) along the radar observation survey line, and the vertical axis represents the two-way traveling time (ns). (b) Radar simulation was calculated by the FDTD algorithm. (c) Constructed lunar regolith model with dimensions of 6.5 × 72.4 m, a background dielectric constant of approximately 3.2, and a standard deviation of approximately 18.8%; the dielectric constant of the discrete layered structures is assumed to be 5.5. The above parameters setting are derived from the actual values obtained through inversion of high-frequency radar data by the Yutu radar [18].

regolith model and imposed constraints on increasing density with depth. We successfully constructed a model spanning approximately 72.4 m in length and 6 m in depth, covering the region from navigation points N105 to N208, as depicted in Fig. 5(c).

After conducting FDTD simulations on this newly developed lunar regolith model, we obtained corresponding radar simulations, as shown in Fig. 6(b). Fig. 6(a) represents actual high-frequency radar observation, which has undergone data processing. Subsequently, we compared the radar observation data with the simulated data, calculating their cosine similarity. The results demonstrated a cosine similarity of approximately 96.21%, indicating significant similarity between them. Therefore, we conclude that the lunar regolith within the top 4 m of the CE-3 landing site indeed exhibits multilayered structures.

The surface of the CE-3 landing area is associated with basal dating to approximately 2.65 Ga old [19], making it a relatively young geological unit overall on the Moon's surface. In younger geological units, the interior maturity of the lunar regolith is generally immature, and it is expected to contain scattered rock fragments. Panoramic camera data from the CE-3 lander confirmed the presence of surface rocks with diameters ranging from 0.07 to 0.28 m, with an estimated surface rock abundance of approximately 1.2% [49], [50]. However, our lunar regolith model did not account for the influence of these rocks. This omission was due to the challenge of accurately locating and quantifying the distribution of rocks in the lunar subsurface at the CE-3 landing site, as well as the uncertainty surrounding their shapes and properties.

During the modeling process, we relied on manual visual methods to extract the discrete layered structures. However, the vertical resolution of the high-frequency radar is approximately 0.3 m, which may have led to slight discrepancies between the extracted layered structures and the actual lunar regolith structure. Nonetheless, these discrepancies fall within an acceptable range. While there may be differences in the fine details between the simulated observation data and actual observations, the overall radar echo characteristics exhibit a high degree of similarity. This supports the conclusion that discrete layered structures exist within the lunar regolith, and these differences do not diminish this fact.

IV. Discussion

A. Consequence of Rock Fragments Within Lunar Regolith on the Discrete Layered Structure

Our result indicates the presence of the discrete layered structure within the shallow subsurface regolith within 4 m at the CE-3 landing site. Previous studies suggested that the material within this shallow subsurface region should consist of ejecta from the Ziwei crater [29], [51]. Ejecta typically comprises a mixture of rock fragments and fine-grained lunar regolith, which contradicts our finding of the discrete layered structure in the shallow subsurface. This discrepancy may arise from previous studies not specifically addressing the similarity between simulated radar data and observed data.

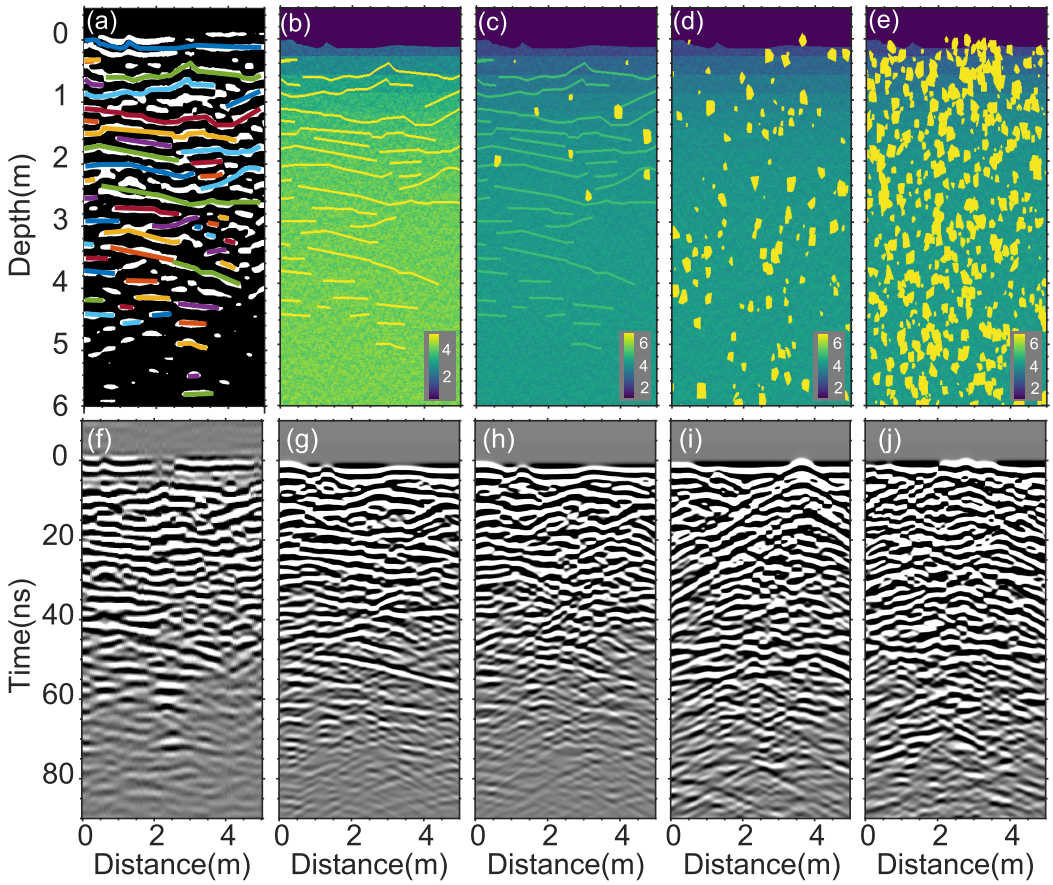

Fig. 7. Examples of the lunar regolith models and their corresponding radar simulations. (a) Different colored line segments in the high-frequency radargram represent the positions of discrete layered structures. (b) Constructed lunar regolith model with discrete layered structures. (c) Randomly adding some rock fragments to the regolith model. (d) Removing the discrete layered structure and randomly adding some rock fragments to the regolith model, with a rock fragment content of approximately 7.59%. (e) Regolith model with a rock fragment content of approximately 30.65%. (f) Radar observation. (g)–(j) Radar simulations of the regolith models in panel (b)–(e), respectively.

To assess the influence of rock fragments on the forward results of the lunar regolith model, we established regolith models, as depicted in Fig. 7(b)–(e), with corresponding radar simulations in Fig. 7(g)–(j). Fig. 7(a) illustrates the process of manually extracting stratified structures from radar observation, while Fig. 7(f) presents the radar observation image.

When we introduced rock fragments into the lunar regolith model, as shown in Fig. 7(c), the echo signals of the discrete layered structure in the radar simulations are locally disrupted, but the echo features of the discrete layered structure were retained. However, when we removed the discrete layered structure within the lunar regolith and introduced approximately 7.59% of rock fragments, creating a model as shown in Fig. 7(d), then we obtained the corresponding radar simulation shown in Fig. 7(i). It demonstrates large curved reflections within the shallow region at a time of 0–20 ns, which did not match the actual observation data [see Fig. 7(f)]. When the rock fragment content within the regolith increased to approximately 30.65%, as depicted in Fig. 7(e), its simulated radar image [see Fig. 7(j)] exhibited some similarity to the actual observation. Certain discrete layered structures are also observable in the radar simulations. This suggests that when the rock fragment content reaches a certain proportion, it may produce radar echo features similar to those observed by the CE-3 high-frequency radar.

However, previous studies have indicated that the dielectric constant within the lunar regolith at a thickness of 4 m at the CE-3 landing site is approximately 3.2 [18], [29]. This indicates that the lunar regolith primarily consists of low-density regolith-like material, rather than the materials dominated by rock fragments. Previous studies indicate that the lunar regolith content within the ejecta of the Ziwei crater ranges from approximately 69.32% to 92.43% [24], [52]. Therefore, the lunar regolith models depicted in Fig. 7(d) and (e) do not align with the actual conditions within the lunar regolith at the CE-3 landing site and can be excluded. Consequently, this study maintains the belief that the horizontal reflectors observed by the CE-3 high-frequency radar are a result of the discrete layered structure within the lunar regolith.

B. Comparison and Analysis of the CE-3 and Apollo 17 Landing Sites

We have identified similarities between CE-3 and Apollo 17 landing sites through image data comparison. Both landing sites are situated on continuous ejecta blankets of impact craters. The Apollo 17 mission landed in the Mare Tranquillitatis region on the near side of the Moon. The Apollo 17 landing site is located approximately 600 m to the east of the Camelot crater's rim [see Fig. 8(b)], while the CE-3

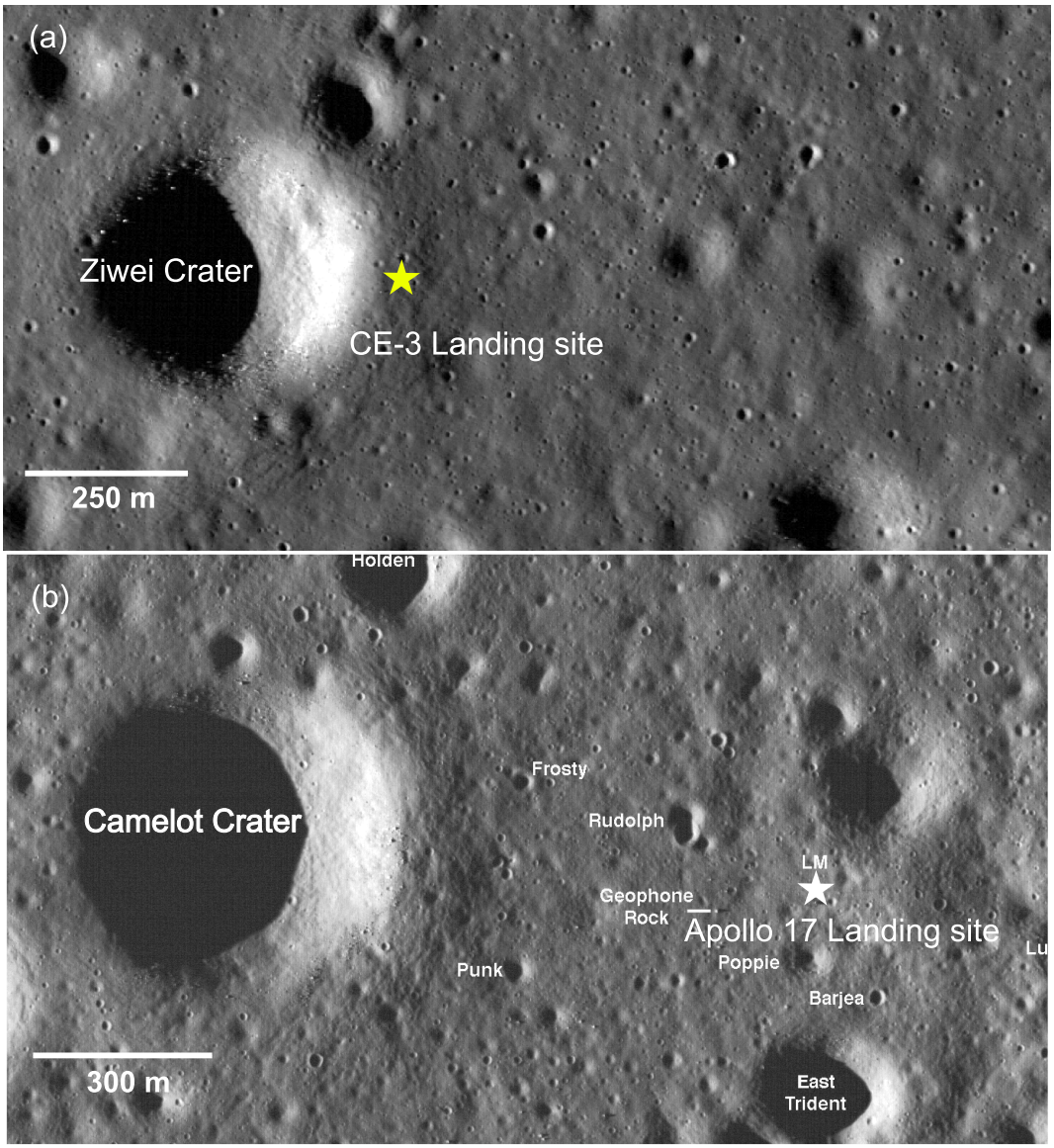

Fig. 8. Geological context maps of the CE-3 and Apollo 17 landing sites. (a) CE-3 landing site, with the landing site located approximately 50 m to the east of the rim of the Ziwei crater with a diameter of 450 m. The landing site is marked with a yellow star. (b) Apollo 17 landing site, with the landing site situated approximately 600 m to the east of the rim of the Camelot crater with a diameter of 650 m. The landing site was marked with a white star.

landing site is situated 50 m to the east of the Ziwei crater's rim [see Fig. 8(a)]. The Camelot crater has a diameter of approximately 650 m, which is comparable in scale to the Ziwei crater with a diameter of approximately 450 m.

Apollo 17 conducted on-site drilling and sampling in the landing area, reaching a drill depth of ∼3 m [15], whereas the CE-3 landing site did not include drilling and sampling activities. However, high-resolution radar observation data within the top 10 m of the shallow subsurface were obtained using GPR technology. Consequently, we can carry out a comparative analysis between the two missions (Fig. 9). Both missions collected data on the lunar subsurface using drilling and radar sensing, allowing for the examination of the interior structure of the regolith.

The age of the Camelot crater has been constrained to be $\leq$ 140 Ma [54], while the Ziwei crater is believed to have formed approximately before 100 Ma [29]. Based on the production equation and the age equation from Neukum et al. [53], we have constrained the age of the Ziwei crater to be 72.04 $\pm$ 0.38 Ma, as shown in Fig. 10. Hence, the ages of both craters are similar. Around the rim of the Ziwei crater, there is a distribution of numerous fragmented rocks of various sizes, as depicted in Fig. 9(a). This geological background is quite similar to that around the Apollo 17 landing site at the Camelot crater, where large fragmented rocks are also distributed, as shown in Fig. 9(b).

The analysis of core samples from drilling indicates the presence of discrete layered structures in the shallow regolith of the Apollo 17 landing site, as illustrated in Fig. 9(c) [55], [56]. These discrete layered structures are interpreted as ejecta from the crater surrounding the Apollo 17 landing site, composed internally of a mixture of fragmented basalt and breccias [56]. Among the contributions to the deposition of discrete layered structures in the shallow regolith, based

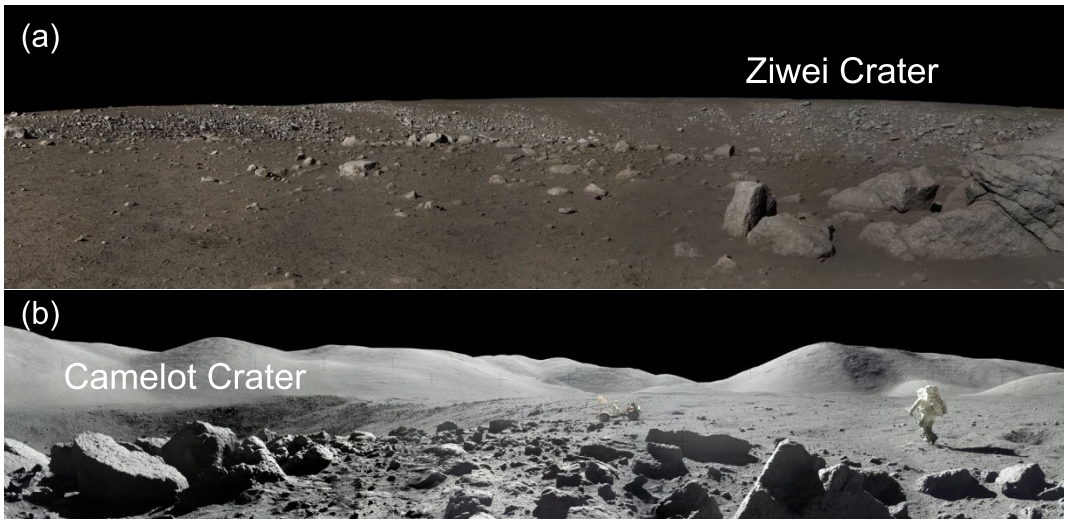

Fig. 9. (a) Image captured by the panoramic camera of the Yutu rover showing the Ziwei crater. Numerous fragmented rocks are distributed around the rim of the crater. (b) Image of the Camelot crater acquired by the Apollo 17 mission, surrounded by numerous fragmented rocks, on the right shows astronauts wandering.

on impact crater principles, the Camelot impact crater's ejecta to the core drilling area are estimated to be approximately between 0.5 and 1.0 m [23]. This suggests that the ejecta from the Camelot crater may belong to one of the discrete layers.

In contrast, the theoretical deposition thickness of ejecta from the Ziwei crater at the CE-3 landing site is estimated to be ∼5 m [51], while radar observations indicate the presence of discrete layered structures within the shallow regolith of up to 4 m. Ejecta are typically mixtures of fragmented rocks and lunar regolith, and it might be challenging for a single event of ejecta to form multiple layers of stratified structures. A reasonable assumption is that the ejecta from the Ziwei crater may not have been deposited within the top 4 m of the shallow subsurface but may have been covered by ejecta from smaller impact events that occurred later.

C. Origin of the Discrete Layered Structures

The origin of the discrete layered structures observed within the lunar regolith through radar observations is not well understood. Generally, lunar regolith is considered to be loose material covering the rocky Moon's surface, primarily formed by meteorite impacts or the weathering of surface materials in space [3]. Data from Apollo core samples have revealed the presence of fine stratified structures within the lunar regolith, with thicknesses ranging from a few centimeters to over ten centimeters [15], [31], [32]. These structures are thought to originate from the crater's ejecta or the deposition of volcanic ash.

Regarding the origin of the discrete layered structures observed in the CE-3 landing area, we propose two hypotheses to speculate on their possible origins. One hypothesis is that they could result from the deposition of multiple layers of lunar volcanic ash over time. Another hypothesis is that they could be formed by the deposition of ejecta from small craters in the vicinity of the landing site.

Hypothesis 1 (Deposition of Volcanic Ash): The surface geological age of the CE-3 landing area is constrained to be approximately 2.5 Ga [19]. The Mare basalt samples returned by the Chang'E-5 mission indicate that lunar volcanic activity persisted until at least 2.0 Ga before [58], [59]. Therefore, after the most recent episode of basalt flow coverage at the CE-3 landing site, there is a high probability that the landing area was covered by volcanic ash from various volcanic eruptions in the surrounding region for at least 0.5 Ga.

In ground validation experiments, the WISDOM radar will be carried out by the European Space Agency's EoxMARS mission to test the multilayered volcanic ash structures at Mount Etna in Italy [60]. Radar images of these stratified volcanic ash deposits displayed horizontal echo features remarkably similar to the structures observed by the Yutu radar observations. Furthermore, in excavations at a Norse farm in Iceland, alternating deep gray or black volcanic sediment layers were found in the glacial till profile, with each layer having a thickness of 0.03–0.056 m, as shown in Fig. 11(b) [57]. This demonstrates the existence of multiple layered structures formed by volcanic ash deposition in surface soils on Earth, and their radar images show similarities to CE-3 high-frequency radar images.

However, there is currently little proof to suggest the presence of volcanic ash deposits within the lunar regolith. The only direct observational evidence comes from the Apollo 17 mission, where a unique core sample (sample 7410012) was collected from the rim of the Shorty crater, which had a diameter of 110 m and a depth of 11 m. This sample revealed orange-colored volcanic ash deposits at the Apollo 17 landing site [61], as shown in Fig. 11(a). This observation appears to support the reasonable inference that the stratified structures discovered within the lunar regolith at the CE-3 landing area may indeed be deposits of volcanic ash.

Although orange-colored volcanic ash deposits were discovered at the Apollo 17 landing site's Shorty crater, this does not invalidate our exclusion of the ash origin of the discrete layered structures. Specifically, as the formation of the Shorty crater postdates the last volcanic eruption, the Apollo

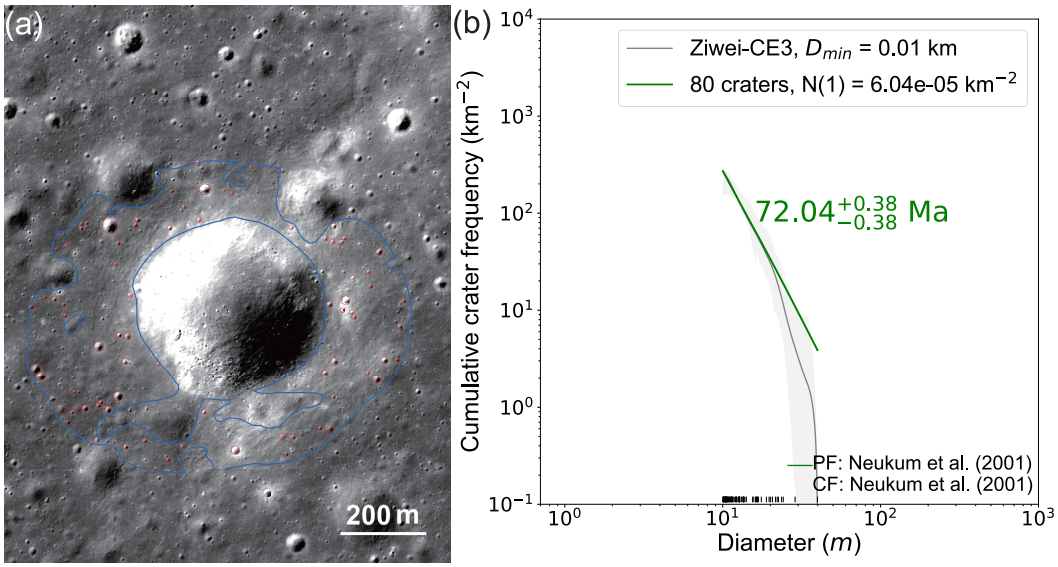

Fig. 10. Dating of the Ziwei crater by crater counting technique. (a) Statistical analysis of craters on the continuous ejecta blanket of the Ziwei crater. The base map has a resolution of 1 m, and we have only included craters with diameters greater than 10 m in our calculations. The blue lines represent the region where the crater was counted, while the red circles indicate the identified craters. (b) Result of crater dating is obtained by using Neukum et al.'s [53] method.

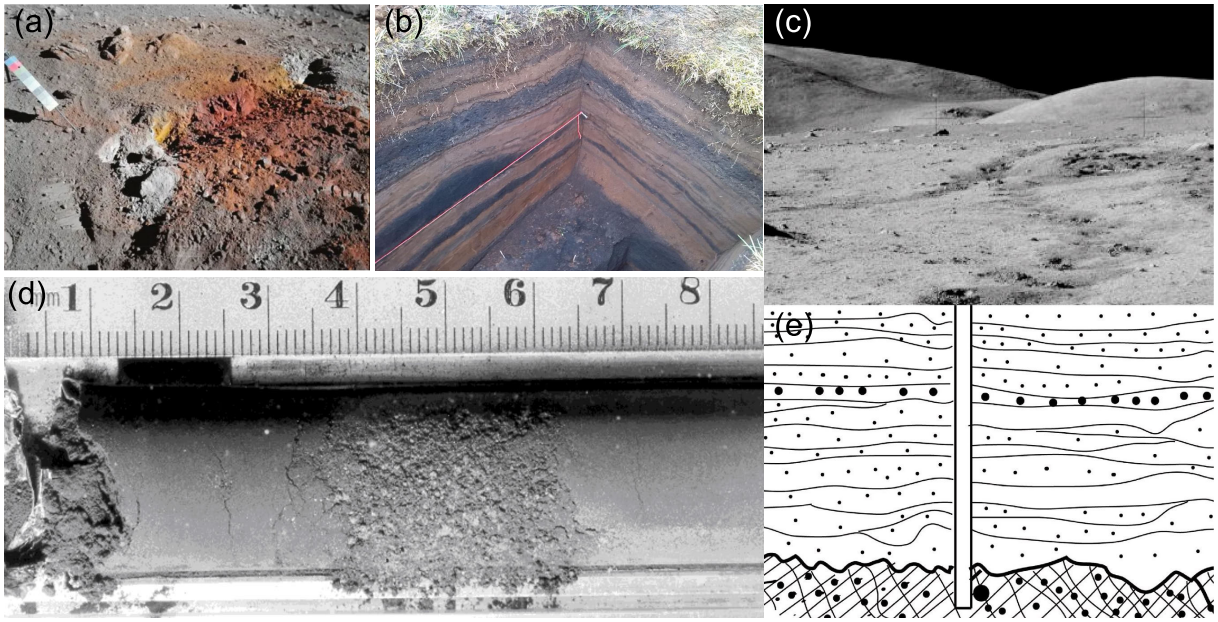

Fig. 11. Stratified structures in the lunar and Earth's shallow subsurface. (a) Orange-colored volcanic ash deposits were discovered in the surface regolith during the Apollo 17 mission (image ID: AS17-137-20984). (b) Multiple layered volcanic ash deposits found in Earth's shallow subsurface [57]. (c) Panoramic image of the lunar surface captured by the Apollo 17 mission [55]. (d) Coarse layer within Apollo core sample 12028, with a thickness of 2 cm (NASA S69-23404). Scale in cm. (e) Conceptual diagram of discrete layered structures in the shallow regolith of the Apollo 17 landing area [55].

17 orange-colored volcanic ash had to be emplaced in the form of ejecta, supporting the origin of the discrete layered structures from ejecta layers.

Hypothesis 2 (Accumulation From Impact Crater's Ejecta): The interior structure of the lunar regolith is highly complex and not entirely predictable in terms of depth. Therefore, it is reasonable to assume that there are discrete layered layers formed by the deposition of ejecta from small craters within the lunar regolith. Similar discrete layered structures have been found in core samples from the Apollo and Luna missions. For instance, in the Apollo 12 landing area, a double-tube core sample (12025–12028) with a penetration depth of 42 centimeters revealed the presence of ten discrete layers [62]. This funding provides the first evidence of the existence of discrete layers in the lunar regolith.

In the Apollo 15 landing area, core samples (15001–15006) with a length of 236 centimeters identified 42 distinct stratified structures [32]. Similarly, a 221-cm core sample from the Apollo 16 landing area revealed 46 discrete layers [31]. In the Apollo 17 landing area, eight geological layers were identified in a 284-cm core sample [15]. In summary, core samples from the Apollo missions showed the presence of numerous discrete layers in the shallow lunar regolith. Likewise, the high-frequency channel radar also observed approximately

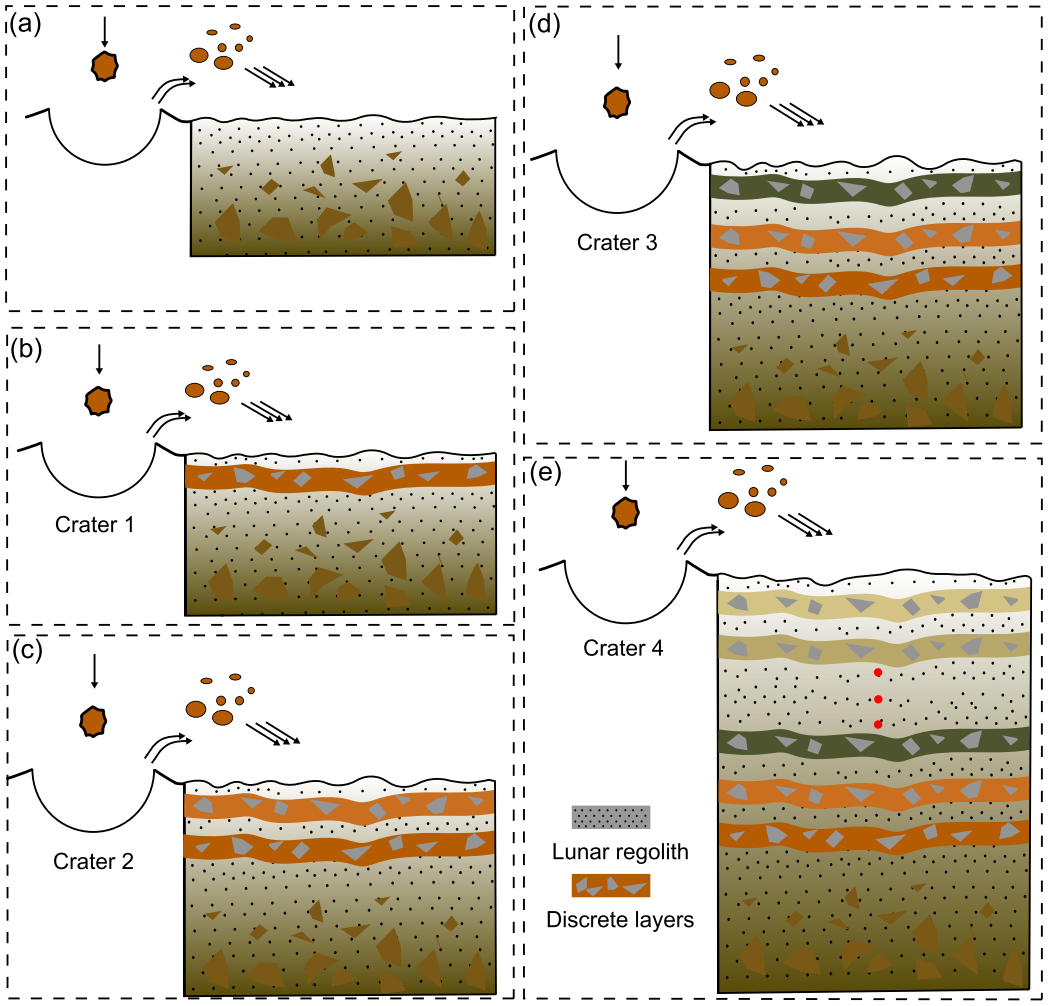

Fig. 12. Geological interpretation of discrete layered structures in the shallow regolith at the CE-3 landing site. (a)–(e) Formation process of discrete layered structures within the shallow regolith up to 4 m deep.

11 discrete layers. There may be more layers, but the vertical resolution of Channel 2 is limited.

The analysis of the Apollo 17 core sample showed that most of the discrete layers were composed of coarse-grained fragmented rocks, which can reasonably be interpreted as ejecta from small craters [as shown in Fig. 9(c)]. Therefore, it is reasonable to speculate that the material within the discrete layers observed by the Yutu radar may also be composed of ejecta from impact craters.

The deposition of volcanic ash within the shallow lunar regolith, as exemplified by the unique cases observed, is presently considered to lack broad representativeness. In this context, we temporarily set aside discussions regarding the origin of the multilayered structure in such cases and focus solely on the formation mechanisms of impact crater ejecta. We hypothesize the formation of the discrete layered structures in the shallow regolith at the CE-3 landing site as follows.

1) Due to the extremely thin atmosphere, meteorites or other rock-like objects can easily impact the lunar surface. Each impact event physically penetrates the lunar surface to different depths, depending on the mass and velocity of the impactor's properties.
2) During the impact cratering process, the material beneath the lunar surface is smashed and excavated, producing ejecta. This physical process typically alters most of the microstratigraphy. Fresh ejecta form a new layer of lunar surface regolith [see Fig. 12(a)].
3) After subsequent meteoroid impacts and solar wind bombardment, the material grain size at the top of the surface layer will become finer and more mature. However, before the surface ejecta have completely weathered into fine-grained regolith, it gets covered by ejecta from subsequent impacts [as shown in Fig. 12(b)]. This cycle repeats with impacts occurring at different times [e.g., Fig. 12(c)–(e)].
4) Eventually, discrete layers are formed in the shallow subsurface of the CE-3 landing site (as shown in Fig. 13). However, it is challenging to identify continuous layers within the regolith from observed radar images, possibly due to lunar surface stirring by meteoroid impacts or shear movements within the shallow subsurface.

In addition, we do not rule out the possibility that the multiple discrete layered structures within the shallow regolith could have been formed by a single impact event. Upon forming the Ziwei crater, kinetic energy was converted to heat, resulting in high temperatures on the lunar surface. This heat melted the lunar surface material, which was then splashed

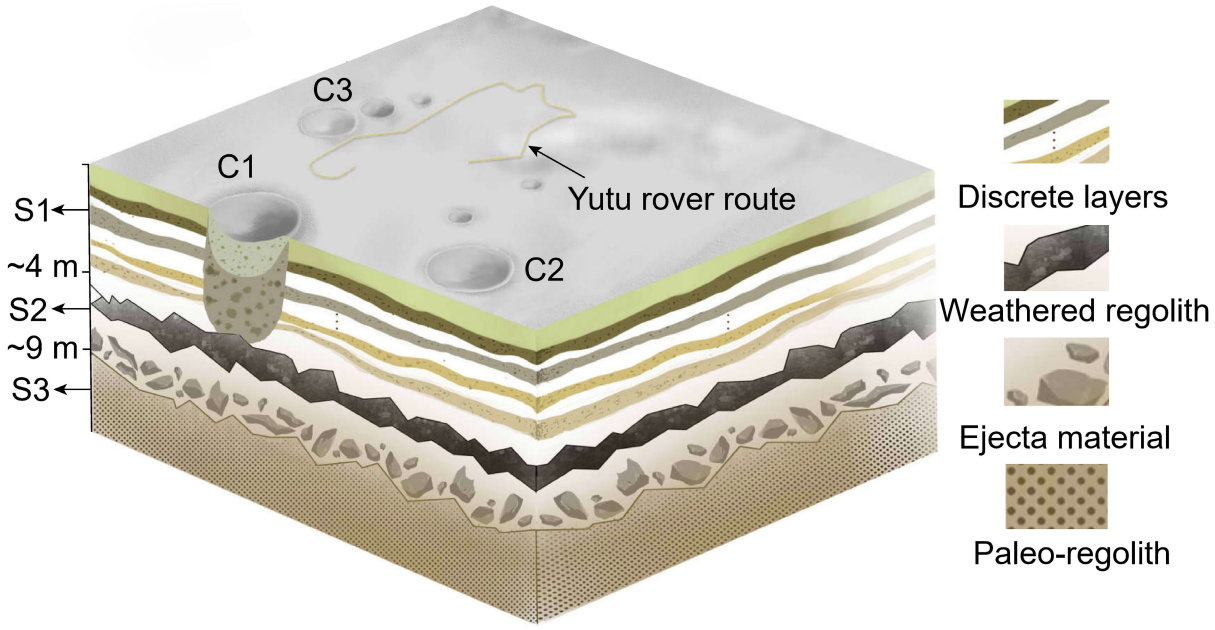

Fig. 13. Schematic illustration of the updated shallow regolith stratification in the CE-3 landing area observed by the Yutu radar. Unit S1 represents the discrete layers within the top 4 m. Unit S2 corresponds to the ejecta from the Ziwei crater, where the surface ejecta may have weathered into fine-grained regolith. Unit S3 represents the paleoregolith predating the formation of the Ziwei crater.

outward along the crater's walls. When these molten materials fell back to the lunar surface and were subjected to horizontal forces, they entrapped into fine-grained regolith forming these discrete layers [18]. Whether the discrete layers observed in this study are composed of ejecta or formed by molten material entrapping fine-grained regolith, or a combination of both, remains a possibility. This may require core drilling and sampling to verify.

This study primarily discusses the discrete layers within the top 4 m of the lunar regolith observed by the Yutu radar, but the structures beneath this depth are not discussed. According to previous findings, the Yutu radar has observed regolith stratification structures beneath the lunar surface to a depth of approximately 9 m [19], [24], [25]. Here, we can reasonably infer that the layer from about 4 to 9 m below the lunar surface consists of ejecta from the Ziwei crater, with the top surface possibly weathered into fine-grained regolith but with an unknown thickness (as shown in Fig. 13). However, the Yutu radar did not obtain effective radar data below approximately 9 m, and Channel 1 also did not detect effective data in the shallow regolith due to signal saturation issues. Here, we reasonably speculate that this layer consists of paleo-regolith material predating the formation of the Ziwei crater, and it may also contain numerous discrete layer structures. However, it has not been observed by the high-frequency radar.

In summary, we conclude that the discrete layers observed within the top 4 m of lunar regolith by the CE-3 high-frequency radar are likely composed of ejecta from small impact craters surrounding the landing area, and it cannot rule out deposits of volcanic ash. Furthermore, according to the broad definition of lunar regolith as loose surface material covering the bedrock of the Moon, the regolith thickness in the CE-3 landing area may exceed approximately 9 m. It surpasses the previously assumed average thickness of 5 m of the lunar regolith in Mare regions. This also highlights the significant contribution of ejecta from small impact craters on the lunar surface to the accumulation of regolith thickness in the landing area.

V. Conclusion

The CE-3 high-frequency radar obtained the lunar regolith structural information at approximately 114 m along the Yutu rover's traveling path. Based on data processing and numerical simulations of Yutu radar data, discrete layers were identified within the top ~4 m of the lunar regolith. A detailed discussion of the origin of these discrete layers within the lunar regolith was conducted. Our study indicates that the formation of these discrete layers within the lunar regolith is more complex than previously thought. The observed discrete layers detected by the high-frequency radar are likely the result of ejecta from small impact craters surrounding the landing area, which formed after the product of the Ziwei crater. Our study also discusses and cannot rule out the volcanic ash deposition hypothesis. Results from Apollo core drilling and CE-3 high-frequency radar observations demonstrate the presence of discrete layers in the lunar regolith. It suggests the widespread existence of discrete layered structures formed by small impact crater's ejecta within the lunar regolith. These shallow regolith structures are expected to exist on the surfaces of other celestial bodies, particularly those that have experienced a significant number of impact events, such as Mars or Mercury. The findings of this study provide new constraints for understanding surface geological processes in the shallow subsurface of the Moon. In addition, it is recommended that future lunar exploration missions in this region collect core samples to validate the physical characteristics of the discrete layers in the lunar regolith as observed by radar.

ACKNOWLEDGMENT

The Chang'E-3 (CE-3) radar data used in this study are available at the Ground Application System of Lunar Exploration, National Astronomical Observatories, Chinese Academy of Sciences (NAOC) (http://moon.bao.ac.cn/searchOrder_pdsData.search).

REFERENCES

[1] I. A. Crawford, "Lunar resources: A review," *Prog. Phys. Geography*, vol. 39, no. 2, pp. 137–167, 2015.

[2] Z. Kopal, "Recent explorations of the moon by spacecraft," *Contemp. Phys.*, vol. 8, no. 4, pp. 331–356, Jul. 1967.

[3] D. S. McKay et al., "The lunar regolith," in *Lunar Sourcebook*. Cambridge, U.K.: Cambridge Univ. Press, 1991, pp. 285–356.

[4] B. Wilcox, M. Robinson, P. Thomas, and B. Hawke, "Constraints on the depth and variability of the lunar regolith," *Meteoritics Planet. Sci.*, vol. 40, no. 5, pp. 695–710, 2005.

[5] W. Fa and M. A. Wieczorek, "Regolith thickness over the lunar nearside: Results from Earth-based 70-cm Arecibo radar observations," *Icarus*, vol. 218, no. 2, pp. 771–787, Apr. 2012.

[6] Y. Shkuratov, "Regolith layer thickness mapping of the Moon by radar and optical data," *Icarus*, vol. 149, no. 2, pp. 329–338, Feb. 2001.

[7] A. T. Basilevsky et al., "Geologic characteristics of the Luna 17/Lunokhod 1 and Chang'E-3/Yutu landing sites, Northwest Mare Imbrium of the Moon," *Planet. Space Sci.*, vol. 117, pp. 385–400, Nov. 2015.

[8] W. D. Carrier III, "Apollo drill core depth relationships," *Moon*, vol. 10, no. 2, pp. 183–194, 1974.

[9] C. Ding et al., "A review of applications of radar-detection techniques in lunar explorations," *Astronomical Res. Technol.*, vol. 12, no. 2, pp. 228–242, 2015.

[10] G.-Y. Fang et al., "Lunar penetrating radar onboard the Chang'e-3 mission," *Res. Astron. Astrophys.*, vol. 14, no. 12, pp. 1607–1622, Dec. 2014.

[11] R. E. Grimm, "New analysis of the Apollo 17 surface electrical properties experiment," *Icarus*, vol. 314, pp. 389–399, Nov. 2018.

[12] C. L. Li et al., "The Chang'e 3 mission overview," *Space Sci. Rev.*, vol. 190, nos. 1–4, pp. 85–101, 2015.

[13] C. Li et al., "The Moon's farside shallow subsurface structure unveiled by Chang'E-4 lunar penetrating radar," *Sci. Adv.*, vol. 6, no. 9, 2020, Art. no. eaay6898.

[14] J. S. Watkins and R. L. Kovach, "Seismic investigation of the lunar regolith," in *Proc. Lunar Sci. Conf.*, vol. 4, 1973, p. 2561.

[15] G. Taylor, R. Warner, and K. Keil, "Stratigraphy and depositional history of the Apollo 17 drill core," in *Proc. Lunar Planet. Sci. Conf.*, vol. 10, 1979, pp. 1159–1184.

[16] T. Ono et al., "Lunar radar sounder observations of subsurface layers under the nearside Maria of the moon," *Science*, vol. 323, no. 5916, pp. 909–912, Feb. 2009.

[17] L. J. Porcello et al., "The Apollo lunar sounder radar system," *Proc. IEEE*, vol. 62, no. 6, pp. 769–783, Jun. 1974.

[18] C. Y. Ding et al., "Layering structures in the porous material beneath the Chang'e-3 landing site," *Earth Space Sci.*, vol. 7, no. 10, 2020, Art. no. e2019EA000862.

[19] L. Xiao et al., "A young multilayered terrane of the northern mare imbrium revealed by Chang'e-3 mission," *Science*, vol. 347, no. 6227, pp. 1226–1229, Mar. 2015.

[20] J. H. Zhang et al., "Volcanic history of the Imbrium basin: A close-up view from the lunar rover Yutu," *Proc. Nat. Acad. Sci. USA*, vol. 112, no. 17, pp. 5342–5347, 2015.

[21] Y. Liu, B. Liu, B. Xu, Z. Liu, K. Di, and J. Zhou, "High precision topographic mapping at Chang'E-3 landing site with multi-source data," *Int. Arch. Photogramm., Remote Sens. Spatial Inf. Sci.*, vol. 40, pp. 157–161, Apr. 2014.

[22] C. Pieters, T. B. McCord, M. P. Charette, and J. B. Adams, "Lunar surface: Identification of the dark mantling material in the Apollo 17 soil samples," *Science*, vol. 183, no. 4130, pp. 1191–1194, 1974.

[23] G. J. Taylor, K. Keil, and R. D. Warner, "Petrology of Apollo 17 deep drill core. I-depositional history based on modal analyses of 70009, 70008, and 70007," in *Proc. 8th Lunar Sci. Conf.*, Houston, TX, USA, vol. 3. New York, NY, USA: Pergamon Press, 1977, pp. 3195–3222.

[24] C. Ding et al., "Moon-based ground penetrating radar derivation of the Helium-3 reservoir in the regolith at the Chang'E-3 landing site," *IEEE J. Sel. Topics Appl. Earth Observ. Remote Sens.*, vol. 16, pp. 2764–2776, 2023.

[25] L. Zhang et al., "A story of regolith told by lunar penetrating radar," *Icarus*, vol. 321, pp. 148–160, Mar. 2019.

[26] J. Feng, Y. Su, C. Ding, S. Xing, S. Dai, and Y. Zou, "Dielectric properties estimation of the lunar regolith at CE-3 landing site using lunar penetrating radar data," *Icarus*, vol. 284, pp. 424–430, Mar. 2017.

[27] J. L. Lai, Y. Xu, X. P. Zhang, and Z. S. Tang, "Structural analysis of lunar subsurface with Chang'E-3 lunar penetrating radar," *Planet. Space Sci.*, vol. 120, pp. 96–102, Jan. 2016.

[28] C. Ding, Z. Xiao, Y. Su, J. Zhao, and J. Cui, "Compositional variations along the route of Chang'e-3 Yutu rover revealed by the lunar penetrating radar," *Prog. Earth Planet. Sci.*, vol. 7, no. 1, pp. 1–11, 2020.

[29] W. Fa, M. Zhu, T. Liu, and J. B. Plescia, "Regolith stratigraphy at the Chang'E-3 landing site as seen by lunar penetrating radar," *Geophys. Res. Lett.*, vol. 42, no. 23, pp. 10179–10187, Dec. 2015.

[30] C. Y. Ding, Z. Y. Xiao, and Y. Su, "A potential subsurface cavity in the continuous ejecta deposits of the Ziwei Crater discovered by the Chang'E-3 mission," *Earth, Planets Space*, vol. 73, no. 1, p. 53, 2021.

[31] M. B. Duke and J. Nagle, *Lunar Core Catalog*. Houston, TX, USA: Lyndon B. Johnson Space Center, 1976.

[32] G. Heiken, R. Morris, D. McKay, and R. Fruland, "Petrographic and ferromagnetic resonance studies of the Apollo 15 deep drill core," in *Proc. 7th Lunar Sci. Conf.*, Houston, TX, USA, vol. 7. New York, NY, USA: Pergamon Press, 1976, pp. 93–111.

[33] Y. Su et al., "Data processing and initial results of Chang'E-3 lunar penetrating radar," *Res. Astron. Astrophys.*, vol. 14, no. 12, pp. 1623–1632, Dec. 2014.

[34] H. B. Zhang et al., "Performance evaluation of lunar penetrating radar onboard the rover of CE-3 probe based on results from ground experiments," *Res. Astron. Astrophys.*, vol. 14, no. 12, pp. 1633–1641, 2014.

[35] S. Dai et al., "Echo simulation of lunar penetrating radar: Based on a model of inhomogeneous multilayer lunar regolith structure," *Res. Astron. Astrophys.*, vol. 14, no. 12, p. 1642, 2014.

[36] S. G. Xing et al., "The penetrating depth analysis of lunar penetrating radar onboard Chang'e-3 rover," *Res. Astron. Astrophys.*, vol. 17, no. 5, p. 046, 2017.

[37] B. Wu et al., "Topographic modeling and analysis of the landing site of Chang'E-3 on the Moon," *Earth Planet. Sci. Lett.*, vol. 405, pp. 257–273, Nov. 2014.

[38] W. D. Carrier, G. R. Olhoeft, and W. Mendell, "Physical properties of the lunar surface," in *Lunar Sourcebook*. Cambridge, U.K.: Cambridge Univ. Press, 1991, pp. 475–594.

[39] L. T. Ikelle, S. K. Yung, and F. Daube, "2-D random media with ellipsoidal autocorrelation functions," *Geophysics*, vol. 58, no. 9, pp. 1359–1372, Sep. 1993.

[40] C. Ding, S. Xiong, J. Li, Y. Su, and S. Huang, "Yutu-2 radar observation of the lunar regolith heterogeneity at the Chang'E-4 landing site," *Astron. Astrophys.*, vol. 664, p. A43, Aug. 2022.

[41] M. Korn, "Seismic waves in random media," *J. Appl. Geophys.*, vol. 29, nos. 3–4, pp. 247–269, 1993.

[42] Z. Jiang, Z. Zeng, J. Li, F. Liu, and W. Li, "Simulation and analysis of GPR signal based on stochastic media model with an ellipsoidal autocorrelation function," *J. Appl. Geophys.*, vol. 99, pp. 91–97, Dec. 2013.

[43] C. Ding et al., "Numerical simulations of the lunar penetrating radar and investigations of the geological structures of the lunar regolith layer at the Chang'E 3 landing site," *Int. J. Antennas Propag.*, vol. 2017, May 2017, Art. no. 3013249.

[44] C. Ding, Z. Xiao, and Y. Su, "A potential subsurface cavity in the continuous ejecta deposits of the Ziwei Crater discovered by the Chang'E-3 mission," *Earth, Planets Space*, vol. 73, no. 1, p. 53, 2021.

[45] C. Y. Ding, Z. Y. Xiao, Y. Su, and J. Cui, "Hyperbolic reflectors determined from peak echoes of ground penetrating radar," *Icarus*, vol. 358, Apr. 2021, Art. no. 114280.

[46] T. Casademont et al., "RIMFAX ground penetrating radar reveals dielectric permittivity and rock density of shallow Martian subsurface," *J. Geophys. Res., Planets*, vol. 128, no. 5, 2023, Art. no. e2022JE007598.

[47] C. H. Dix, "Seismic velocities from surface measurements," *Geophysics*, vol. 20, no. 1, pp. 68–86, Jan. 1955.

[48] J. Ye, "Cosine similarity measures for intuitionistic fuzzy sets and their applications," *Math. Comput. Model.*, vol. 53, no. 1, pp. 91–97, 2011.

[49] K. Di et al., "Rock size-frequency distribution analysis at the Chang'E-3 landing site," *Planet. Space Sci.*, vol. 120, pp. 103–112, Jan. 2016.
[50] Y. Li and B. Wu, "Analysis of rock abundance on lunar surface from orbital and descent images using automatic rock detection," *J. Geophys. Res., Planets*, vol. 123, no. 5, pp. 1061–1088, 2018.
[51] L. Qiao, Z. Y. Xiao, J. N. Zhao, and L. Xiao, "Subsurface structures at the Chang'e-3 landing site: Interpretations from orbital and in-situ imagery data," *J. Earth Sci.*, vol. 27, no. 4, pp. 707–715, 2016.
[52] C. Ding et al., "Electromagnetic signal attenuation characteristics in the lunar regolith observed by the lunar regolith penetrating radar (LRPR) onboard the Chang'E-5 lander," *Remote Sens.*, vol. 14, no. 20, p. 5189, 2022.
[53] G. Neukum, B. A. Ivanov, and W. K. Hartmann, "Cratering records in the inner solar system in relation to the lunar reference system," in *Proc. Chronol. Evol. Mars: Workshop (ISSI)*. Bern, Switzerland: Springer, 2001, pp. 55–86.
[54] R. Arvidson, G. Crozaz, R. Drozd, C. Hohenberg, and C. Morgan, "Cosmic ray exposure ages of features and events at the Apollo landing sites," *Moon*, vol. 13, pp. 259–276, Mar. 1975.
[55] M. Y. Marov and E. N. Slyuta, "Early steps toward the lunar base deployment: Some prospects," *Acta Astronautica*, vol. 181, pp. 28–39, Apr. 2021.
[56] K. Renner, "Apollo 17: Preliminary science report," Nat. Aeronaut. Space Admin. (NASA), Washington, DC, USA, Tech. Rep. 7, 1973.
[57] N. A. Cutler, O. M. Shears, R. T. Streeter, and A. J. Dugmore, "Impact of small-scale vegetation structure on tephra layer preservation," *Sci. Rep.*, vol. 6, p. 37260, Nov. 2016.
[58] Y. Chen et al., "Chang'e-5 lunar samples shed new light on the Moon," *Innov. Geosci.*, vol. 1, no. 1, 2023, Art. no. 100014.
[59] Q.-L. Li et al., "Two-billion-year-old volcanism on the Moon from Chang'e-5 basalts," *Nature*, vol. 600, no. 7887, pp. 54–58, 2021.
[60] V. Ciarletti et al., "The WISDOM radar: Unveiling the subsurface beneath the ExoMars Rover and identifying the best locations for drilling," *Astrobiology*, vol. 17, nos. 6–7, pp. 565–584, 2017.
[61] E. W. Wolfe et al., "The geological investigation of the taurus-littrow valley: Apollo 17 landing site," U.S. Geol. Surv., Washington, DC, USA, Tech. Rep. 77-783, 1977.
[62] G. Heiken, D. Vaniman, and B. M. French, *Lunar Sourcebook: A User's 1007 Guide to the Moon*. Cambridge, U.K.: Cambridge Univ. Press, 1991.

Chunyu Ding received the Ph.D. degree in astronomy from the University of Chinese Academy of Sciences, Beijing, China, in 2017.

He has been an Assistant Professor with the Institute of Advanced Study, Shenzhen University, Shenzhen, China, since 2021. He is a Core Scientific Member of the Chinese ChangE-4 Mission and also involved in the team on the radar group of the Chinese First Mars Mission, Tianwen-1. His research interests focus on the radar detection of terrestrial planets and the surface evolution of terrestrial bodies in the solar system, e.g., the Moon and Mars.

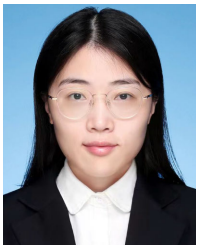

Yiren Chang received the Ph.D. degree in information technology from the Macau University of Science and Technology, Macau, China, in 2021.

She has been a Lecturer with Shanghai Normal University, Shanghai, China, since 2021. She is a Core Scientific Member of the Chinese Chang'E-5 Mission. Her research interests focus on excluding the effect of background secondaries in crater statistical methods and the surface evolution of terrestrial bodies in the solar system, e.g., the Moon and Mars.

Yan Su received the Ph.D. degree in astronomical techniques and methodology from the National Astronomical Observatories, Chinese Academy of Sciences (CAS), Beijing, China, and The University of Manchester, Manchester, U.K., in 2003, under the Joint Doctoral Program.

Since 2012, she has been a Professor with the National Astronomical Observatories, CAS. Her research interests include ground-penetrating radar data processing and interpretation, developing downlink ground stations for Chinese deep space exploration, and microwave radiometer applications for planetary investigations.

Jiawei Wang is currently pursuing the bachelor's degree in physics with Shenzhen University, Shenzhen, China.

In 2021, he studied at the Institute of Advanced Research, Shenzhen University. His main research is planetary radar astronomy.

Minggang Xie received the Ph.D. degree in space information technology from the Macau University of Science and Technology, Macau, China, in 2016.

He has been an Associate Professor with the School of Physics and Electronic Information Engineering, Guilin University of Technology, Guilin, China, since 2020. His research interests include impact cratering, topography evolution, and near-Earth objects.